Review of Scientific Instruments ARTICLE scitation.org/journal/rsi

Bremsstrahlung cannon design for shock ignition relevant regime

Cite as: Rev. Sci. Instrum. 92, 013501 (2021); doi: 10.1063/5.0022030
Submitted: 16 July 2020 • Accepted: 11 December 2020 •
Published Online: 4 January 2021

P. Koester,[1,a] F. Baffigi,[1] G. Cristoforetti,[1] L. Labate,[1] L. A. Gizzi,[1,a] S. Baton,[2] M. Koenig,[2] A. Colaïtis,[3] D. Batani,[3] A. Casner,[3] D. Raffestin,[3] A. Tentori,[3] J. Trela,[3] C. Rousseaux,[4] G. Boutoux,[4] S. Brygoo,[4] L. Jacquet,[4] C. Reverdin,[4] E. Le Bel,[5,b] L. Le-Deroff,[5] W. Theobald,[6] and K. Shigemori[7]

AFFILIATIONS

[1]Intense Laser Irradiation Laboratory, Istituto Nazionale di Ottica, Consiglio Nazionale delle Ricerche, Via G. Moruzzi 1, 56124 Pisa, Italy
[2]Laboratoire pour l'Utilisation des Lasers Intenses, LULI, CNRS-Ecole Polytechnique-CEA-Sorbonne Universités, UMR 7605, F-91128 Palaiseau, France
[3]Centre Lasers Intenses et Applications, CELIA, Université de Bordeaux-CNRS-CEA, UMR 5107, F-33405 Talence, France
[4]Commissariat á l'energie Atomique et aux Énergies Alternatives, CEA, Direction des Applications Militaires, DAM, Île-de-France, F-91297 Arpajon, France
[5]Commissariat á l'energie Atomique et aux Énergies Alternatives, CEA, Direction des Applications Militaires, DAM, Centre d'études Scientifiques et Techniques d'Aquitaine, CESTA, F-33114 Le Barp, France
[6]Laboratory for Laser Energetics, University of Rochester, Rochester, New York 14623, USA
[7]Institute of Laser Engineering, University of Osaka, Osaka 565-0871, Japan

[a]**Authors to whom correspondence should be addressed:** petra.koester@ino.cnr.it and leonidaantonio.gizzi@ino.cnr.it
[b]**Also at:** Centre Lasers Intenses et Applications, CELIA, Université de Bordeaux-CNRS-CEA, UMR 5107, F-33405 Talence, France.

ABSTRACT

We report on the optimization of a BremsStrahlung Cannon (BSC) design for the investigation of laser-driven fast electron populations in a shock ignition relevant experimental campaign at the Laser Megajoule-PETawatt Aquitaine Laser facility. In this regime with laser intensities of 10^{15} W/cm^2–10^{16} W/cm^2, fast electrons with energies ≤100 keV are expected to be generated through Stimulated Raman Scattering (SRS) and Two Plasmon Decay (TPD) instabilities. The main purpose of the BSC in our experiment is to identify the contribution to x-ray emission from bremsstrahlung of fast electrons originating from SRS and TPD, with expected temperatures of 40 keV and 95 keV, respectively. Data analysis and reconstruction of the distributions of x-ray photons incident on the BSC are described.

I. INTRODUCTION

In the Shock Ignition (SI) approach to Inertial Confinement Fusion (ICF), the compression phase and ignition phase are separated.[1] In the first phase, symmetric laser irradiation compresses the outer shell of the fuel capsule, generating a large-scale plasma corona. After compression, a laser intensity spike is envisaged to drive a strong shock (~300 Mbar) in the precompressed fuel capsule to generate ignition conditions. In order to produce such a strong shock, the laser intensity must reach values of 10^{15} W/cm^2–10^{16} W/cm^2. It is well-known[2] that in this interaction regime, parametric instabilities such as Stimulated Raman Scattering (SRS),[3–6] Two Plasmon Decay (TPD),[5,7] and Stimulated Brillouin Scattering (SBS)[8,9] are driven in the long-scale-length plasma generated during the compression phase. These instabilities result in reflected laser light (SRS, SBS) and the generation of non-thermal electron populations (SRS, TPD),[10] the so-called fast electrons. One of the major open issues within the SI approach is the effect of the fast electrons on the ability to drive a strong shock.[11] On the one hand, the fast electrons might have the detrimental effect of preheating the precompressed fuel, resulting in less efficient shock formation. On the other hand, low energy fast electrons (<100 keV) can be

stopped inside the high-density precompressed shell enhancing the shock formation.[12] Measuring the fast electron properties (conversion efficiency, temperature) simultaneously with the shock pressure is, therefore, of great importance in the SI relevant regime.

Fast electron properties have been studied through direct measurement of the escaping component of fast electrons with magnetic dipole spectrometers[13] or via dosimetric techniques[14] and indirect measurements such as bremsstrahlung x-ray measurements[15,16] and measurements of K_α emission,[17,18] also from buried fluorescent layers at different depths inside the target.[19] In the experimental conditions considered here, the target is thick with respect to the CSDA (Continuous Slowing Down Approximation) stopping range of the electron energies. Thus, the direct measurement of the fast electron energies with a magnetic dipole spectrometer is not suitable, as only electrons exiting the target can be detected. The other two diagnostic techniques have been used in the experiment carried out at the Laser Megajoule-PETawatt Aquitaine Laser (LMJ-PETAL) facility. Here, we focus on the bremsstrahlung measurements. The discussion of the results from fluorescence emission can be found elsewhere.[20]

BremsStrahlung Cannons (BSCs) have been widely used in relativistic laser–matter interaction studies with thin targets.[21–24] In that case, the CSDA range of the major part of the fast electrons largely exceeds the target thickness, mainly because of the much higher fast electron temperatures. The fast electron energy loss inside the target can be neglected, and the integration of the bremsstrahlung cross section over the fast electron distribution (usually assumed to be Maxwellian) yields a good approximation[15] of the bremsstrahlung emission produced. In the experimental conditions considered here, most of the fast electrons are stopped inside the target of mm-thickness. Electron energy losses, secondary particle generation, and bremsstrahlung reabsorption inside the target need to be taken into account. Thus, Monte Carlo simulations are used to link the fast electron population to its bremsstrahlung spectrum for the calculation of the expected photon distribution emitted from the target.

Here, we concentrate on the first phase of the data analysis, i.e., the reconstruction of the x-ray photon spectrum entering the BSC. The retrieval of the fast electron distribution from the photon spectrum will be the subject of the future work. The analysis procedure for the retrieval of the photon distribution follows those reported in previous studies.[22,25] Similarly to those works, a response function base is constructed. While the response functions in Refs. 22 and 25 were constructed for incoming photon energy bins, here, a base of Maxwell–Boltzmann photon distributions in a range of temperatures is used. It was shown that the fast electrons produced through parametric instabilities can be well approximated with multi-temperature Maxwellian distributions.[26] Therefore, the bremsstrahlung photon distribution originating from the interaction of the fast electrons with the target material is expected to be well approximated by a multi-temperature Maxwell–Boltzmann distribution. In Ref. 22, the response function was calculated using one-dimensional Monte Carlo simulations, whereas, in Ref. 25, the cumulative transmission of the filters in the BSC stack was calculated for a large parameter space. In the study reported here, the BSC response is calculated using three-dimensional Monte Carlo simulations, which take into account secondary particle emission and reabsorption inside the BSC stack, its housing, and its shielding.

This paper is structured in the following way: In Sec. II, we describe the optimization of the BSC for the detection of the expected bremsstrahlung spectrum. In Sec. III, we explain the analysis procedure. In Sec. IV, we report the first experimental results obtained with the BSC design. In Sec. V, conclusions are drawn.

II. BREMSSTRAHLUNG CANNON DESIGN FOR SI RELEVANT REGIME

In the typical BSC design, a stack of Image Plate (IP) layers, separated by appropriately selected filters, is used to detect x-ray photons.[21–23,25] The stack is enclosed in a container and shielded against scattered radiation, as well as electrons escaping the target. After exposure, IPs are scanned to retrieve the deposited dose, layer by layer. The selection of the filter materials and thicknesses is optimized for the expected photon distribution, as described in the following.

In our experiment, the expected peak laser intensity is 7×10^{15} W/cm^2. In this interaction regime, the electron distribution function expected from simulations can be well approximated by a three-temperature Maxwellian distribution. In particular, fast electrons with a temperature T given by k_BT = 45 keV are expected to be generated through SRS with a conversion efficiency from the laser energy to the electron kinetic energy of 6%–10%, the second component (k_BT = 95 keV) is due to TPD with an expected conversion efficiency of 1.5%–2.5%, and the third component originates from thermal plasma electrons with an expected temperature of k_BT of 4 keV–5 keV. The main objective guiding the design of the BSC stack is the possibility to distinguish between the two contributions originating from SRS and TPD and to measure their respective fast electron temperatures and conversion efficiencies.

In order to optimize the bremsstrahlung cannon stack of filters and IPs, the expected signal in each IP layer is estimated through Monte Carlo simulations with GEANT4[27] using the Penelope low energy electromagnetic physics model,[28] which best reproduces bremsstrahlung emission from low energy (<3 MeV) electrons.[29] The simulations are set up using the detailed geometry of the target and its holder as well as the BSC and its cassette holder. In these simulations, the contribution originating from thermal plasma electrons is neglected, as the low energy bremsstrahlung photons will deposit their energy in the very first layers of the stack only. A two-step procedure was followed: In the first step, Maxwellian fast electron distributions with the expected temperatures due to SRS and TPD instabilities are separately taken as input to the GEANT4 simulations, and the resulting x-ray photon distribution (predominantly bremsstrahlung emission) at the entrance of the BSC stack is retrieved.

In the second step, the resulting photon distributions are parameterized and used separately as input to GEANT4 simulations of the BSC stack, and the deposited energy per simulated photon in each IP active layer is measured in the simulations. The results are then multiplied by the expected photon numbers and converted to PhotoStimulated Luminescence (PSL)/pixel for a pixel size of 100×100 μm^2. Simulations are run for various configurations of filter materials and thicknesses, in order to optimize the stack configuration for enhanced differences between the signal originating

TABLE I. Filter materials and thicknesses before each IP layer of the BSC stack configuration.

Filter no.	Material	Thickness (mm)	Filter no.	Material	Thickness (mm)	Filter no.	Material	Thickness (mm)
1	Al/Mo	2.0/2.0	10	Ta	0.100	19	Pb	1.0
2	Al	0.090	11	Ta	0.100	20	Pb	1.0
3	Ti	0.125	12	Au	0.250	21	Pb	1.0
4	Fe	0.125	13	Au	0.250	22	Pb	1.0
5	Cu	0.100	14	Pb	0.250	23	Pb	1.0
6	Mo	0.100	15	Pb	0.250	24	Pb	1.0
7	Ag	0.150	16	Pb	0.500	25	Pb	6.0
8	Ag	0.300	17	Pb	0.500			
9	Ag	0.300	18	Pb	1.0			

from SRS and TPD bremsstrahlung photons. The filters are optimized to ensure sufficient sampling of the high energy region of the photon distribution, where the TPD component with an expected temperature of 95 keV dominates the signal in the IP active layers.

The optimized stack comprises 25 disk-shaped IPs and filters with increasing attenuation between the IPs, as shown in Table I. This relatively large number of IP layers was chosen in order to allow for the retrieval of a three-temperature distribution from the experimental data. To widen the dynamic range of our BSC, the stack was split into two channels by placing two different half circle filters in front of the optimized stack, one consisting of 2 mm of Al (Al filter channel) and the other of 2 mm of Mo (Mo filter channel), as shown in Fig. 1.

In the graphs of Figs. 2 and 3, the resulting signal in the different IP layers for the expected incoming photon distributions (Fig. 4) is shown. As shown in the graphs, the low energy component is strongly attenuated in the plot of Fig. 3, due to the presence of the Mo filter. Most importantly, in both channels, the signal in the IP layers up to layer 15 is mainly due to SRS, while, from layer 15 onward, it is dominated by the TPD component, despite the much weaker incident TPD signal, nearly one order of magnitude less than

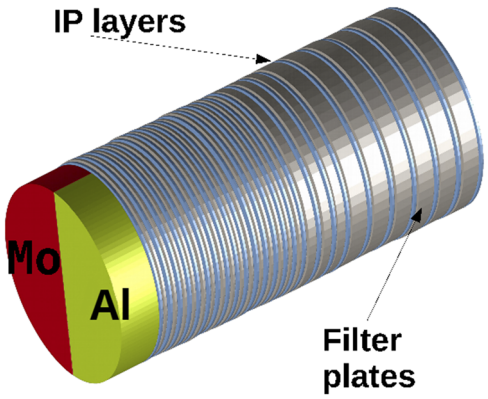

FIG. 1. Schematic view of the bremsstrahlung cannon stack with a split front filter.

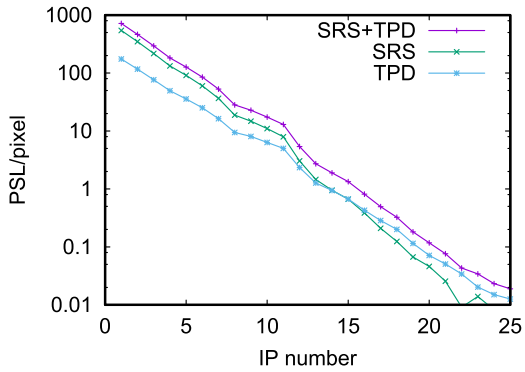

FIG. 2. Calculated response [PhotoStimulated Luminescence (PSL)/pixel] of the 25 Image Plate (IP) layers in the designed bremsstrahlung cannon stack with a 2 mm Al front filter (Al filter channel) for the expected incoming bremsstrahlung photon distribution originating from Stimulated Raman Scattering (SRS) and Two Plasmon Decay (TPD) electrons.

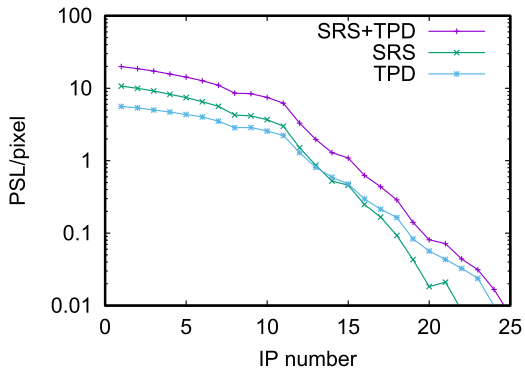

FIG. 3. Calculated response [PhotoStimulated Luminescence (PSL)/pixel] of the 25 Image Plate (IP) layers in the designed bremsstrahlung cannon stack with a 2 mm Mo front filter (Mo filter channel) for the expected incoming bremsstrahlung photon distribution originating from Stimulated Raman Scattering (SRS) and Two Plasmon Decay (TPD) electrons.

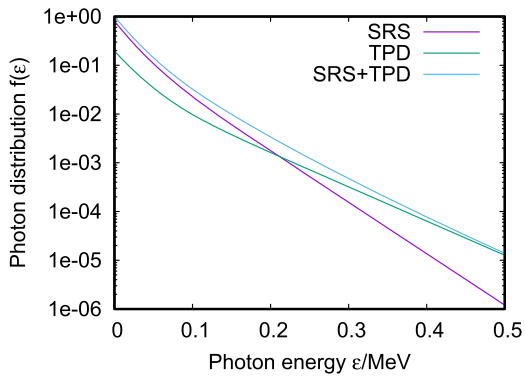

FIG. 4. Expected photon distribution function due to bremsstrahlung photons originating from Stimulated Raman Scattering (SRS) and Two Plasmon Decay (TPD) electrons.

the incident SRS signal. This behavior in the SRS and TPD signals vs IP layer is key to the identification of their respective contributions.

III. DATA ANALYSIS PROCEDURE

A. Data extraction

The IPs (Fujifilm BAS-MS) are scanned after exposure with a GE Typhoon 7000 flatbed IP scanner. The IP scanner stores the scanned values in square-root encoded 16-bit files. The PSL/pixel values are then obtained from the scans by applying the following formula:[30]

$$PSL = \left(\frac{R}{100}\right)^2 \left(\frac{P_{GE}}{2^D - 1}\right)^2 h(V) 10^{L/2}, \tag{1}$$

where R indicates the spatial resolution in μm, L is the dynamic range latitude, P_{GE} is the scanned pixel value, D is the bit depth of the scanned image, and $h(V)$ is an empirically determined function of the photomultiplier tube voltage V applied during the readout process. We observe that the first IP layers of the Al filter channel showed saturation during the first scan, so additional successive scans were necessary until no saturation was present. In fact, the dynamic range of the IPs is larger than the dynamic range of the IP scanner, and each successive scan lowers the signal,[31] so that the full dynamic range can be recovered by successive scans.

The signal is then extracted by selecting an area in the central part of the half circle of each channel and removing the edges potentially affected by noise due to cutting imperfections or rescattering from the BSC walls. The mean and the standard deviation of the signal are calculated for the selected area for each scan. For the dataset of the first shot, the exponential decrease in the signal during successive scans was verified for the various IP layers. Thus, for the IPs showing saturation in the first scan, the signal is reconstructed using the ratio of the signal mean between the first and the last scan for non-saturated IP layers,

$$PSL(k)_{first\ scan} = \frac{PSL(j)_{first\ scan}}{PSL(j)_{last\ scan}} PSL(k)_{last\ scan}. \tag{2}$$

B. Reconstruction of the bremsstrahlung photon distribution

The photon distribution $f(\epsilon)$ impinging on the bremsstrahlung cannon stack is obtained with the assumption that it mainly consists of bremsstrahlung photons and can be approximated with a sum of Maxwell–Boltzmann distributions with N_T temperatures T_j,

$$f(\epsilon) = \sum_{j=1}^{N_T} \beta_j \frac{1}{\kappa T_j} \exp^{-\frac{\epsilon}{\kappa T_j}}, \tag{3}$$

where ϵ indicates the photon energy and κ is the Boltzmann constant.

Thus, through Monte Carlo simulations, a response function base for the BSC stack is built using exponential photon distributions

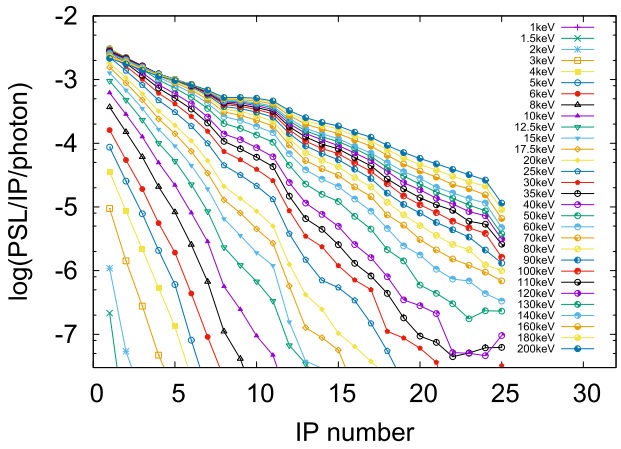

FIG. 5. Calculated response curves [PhotoStimulated Luminescence (PSL)/Image Plate (IP)/photon] of the 25 image plate layers in the bremsstrahlung cannon stack to a single-temperature Maxwell–Boltzmann photon distribution for temperatures in the range 1 keV–200 keV for the Al filter channel.

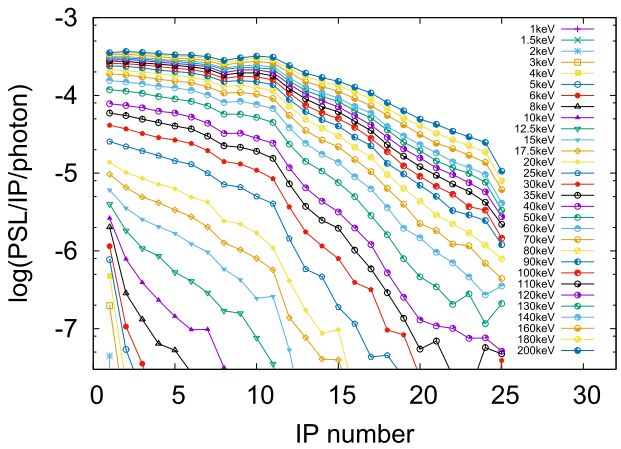

FIG. 6. Calculated response curves [PhotoStimulated Luminescence (PSL)/Image Plate (IP)/photon] of the 25 image plate layers in the bremsstrahlung cannon stack to a single-temperature Maxwell–Boltzmann photon distribution for temperatures in the range 1 keV–200 keV for the Mo filter channel.

for a discrete set of temperatures $\{T_j\}$ in the range between 1 keV and 200 keV for both the Al and Mo filter channels. The energy deposition obtained per incoming photon $E_l^{T_j}$ vs IP number l is shown in the graphs in Figs. 5 and 6.

In order to find the photon distribution that best fits the measured energy deposition on the different IP layers of the BSC stack, the WSSR (Weighted Sum of Squared Residuals) is evaluated for each subset of N_T temperatures T_j as

$$WSSR(\{T_j\}) = \sum_{k=1}^{N_{IP}} \frac{(PSL(k)C_f C_{cal} N_P - \sum_{j=1}^{N_T} \beta_j E_k^{T_j})^2}{(Std(k)C_f C_{cal} N_P)^2}, \quad (4)$$

where N_{IP} is the number of IPs, $PSL(k)$ is the measured PSL mean value per pixel on the k-th IP, C_f (=1.67 for MS-type IP) accounts for fading of the IP due to the time elapsed between exposure and readout of the IP,[32] C_{cal} (=1.33 MeV/PSL) is the calibration constant

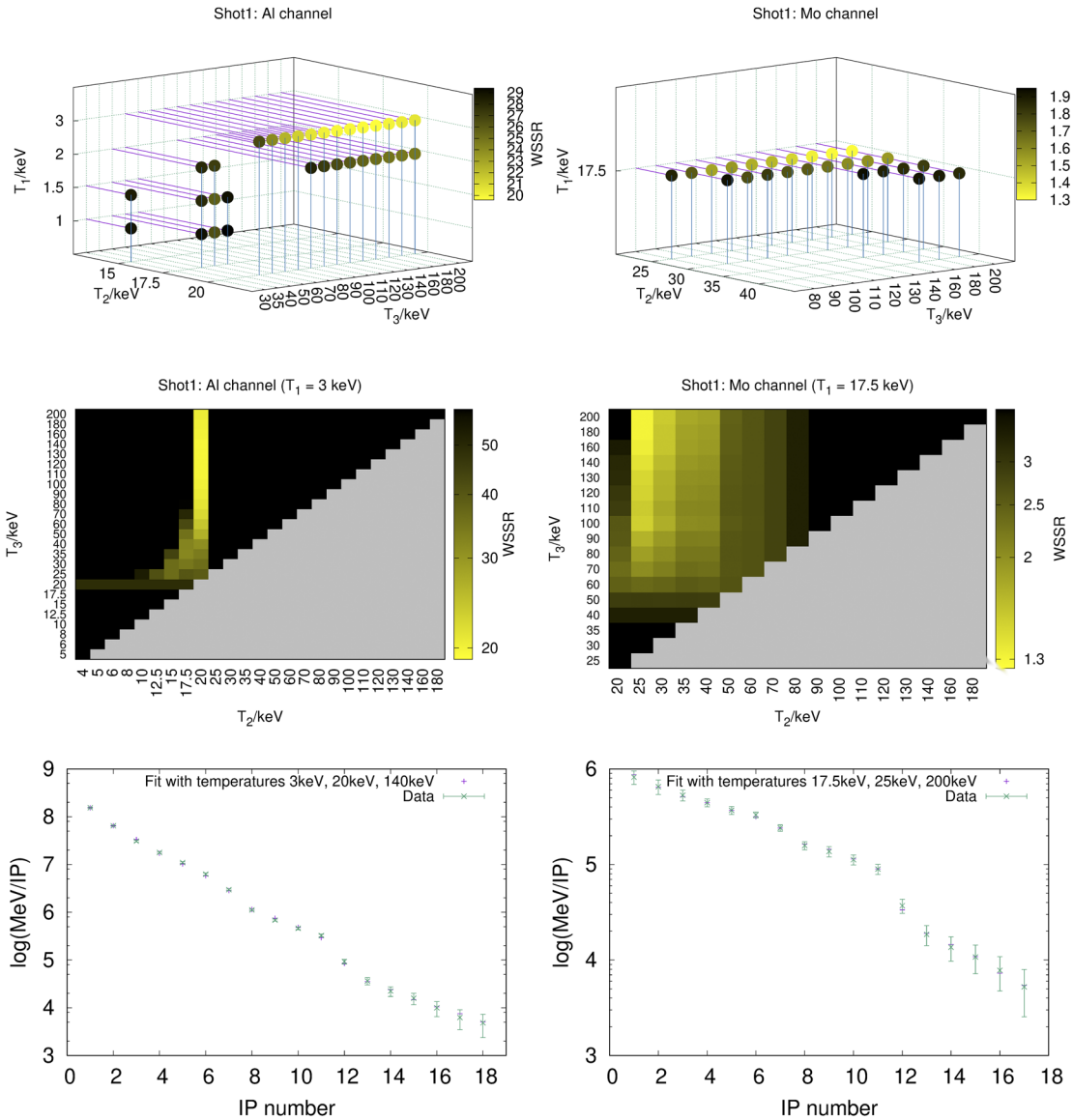

FIG. 7. Shot 1: WSSR for temperature triplets T_1, T_2, and T_3 for the Al filter channel (top left) and the Mo filter channel (top right) and for temperature pairs T_2 and T_3 at fixed T_1 (middle panels). In the bottom panels, the experimental data are shown together with the best fit (minimum WSSR) for the Al (left) and the Mo (right) filter channel.

relating measured PSL values to the deposited energy in MeV,[33] N_P is the number of pixels on an IP, and $E_k^{T_j}$ is the energy (in MeV) deposited on the k-th IP for an incoming photon distribution with temperature T_j as retrieved from Monte Carlo simulations. β_j are the parameters for fitting and indicate the photon number of the exponential photon distribution with temperature T_j, which best fit the experimental data. The WSSR is minimized for each subset of temperatures $\{T_j\}$. The minimum WSSR of each subset of temperatures is registered, and the minimum value among all minimized WSSR values is found. The corresponding subset of N_T temperatures is the set of temperatures best fitting the experimental data. The coefficients β_j, which minimize the WSSR for this subset of temperatures, give the number of photons of the photon distributions with temperatures T_j. Considering the solid angle subtended by the BSC in the experimental geometry, the number of photons/steradian emitted from the target is calculated.

IV. RESULTS AND DISCUSSION

In the experiment at LMJ-PETAL, three shots were delivered with a laser intensity around 2.5×10^{15} W/cm^2, less than the expected intensity due to non-perfect beam overlapping. The first

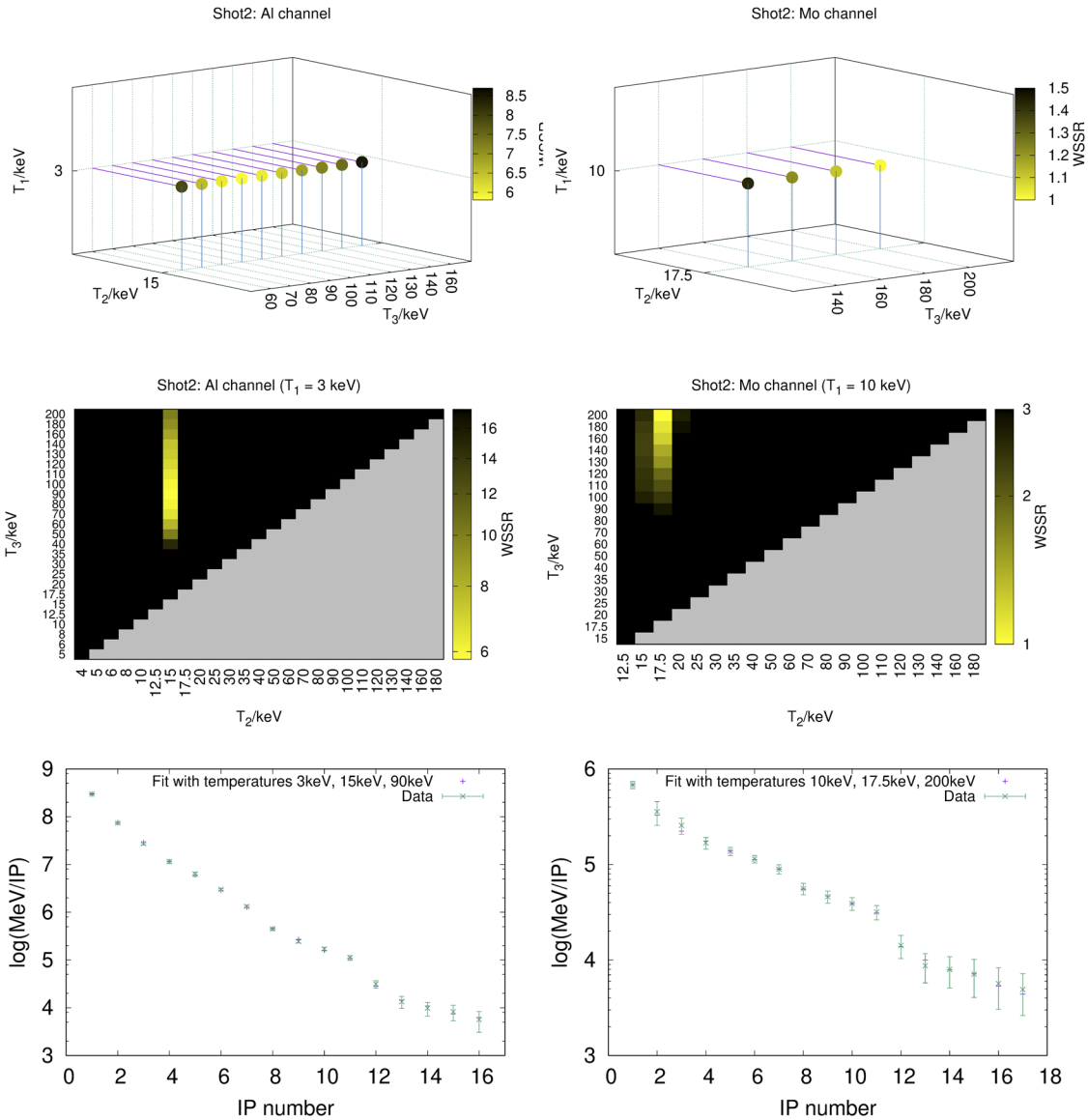

FIG. 8. Shot 2: WSSR for temperature triplets T_1, T_2, and T_3 for the Al filter channel (top left) and the Mo filter channel (top right) and for temperature pairs T_2 and T_3 at fixed T_1 (middle panels). In the bottom panels, the experimental data are shown together with the best fit (minimum WSSR) for the Al (left) and the Mo (right) filter channel.

two shots were delivered on the target without Smoothing by Spectral Dispersion (SSD) of the beam, whereas, for the third shot, SSD was turned on. The BSC was fitted onto the end of the Cassette Radiographic Centre Chambre (CRACC) diagnostic, situated at an angle of 58.5° with respect to the target normal opposite to the laser-irradiated target side. The distance to the target was 26.6 cm for the first two shots and 17.6 cm for the third shot. More details on the experimental setup and results from further diagnostics can be found elsewhere.[20]

The data points were fitted with a three-temperature x-ray photon distribution,

$$f(\epsilon) = \sum_{i=1}^{3} \frac{N_i}{\kappa T_i} \exp^{-\frac{\epsilon}{\kappa T_i}}, \tag{5}$$

where N_i is the photon number per steradian in the Maxwell–Boltzmann distribution with temperature given by κT_i. In Figs. 7–9, the results from the data analysis are shown for the three shots. The top panels in the figures show the minimum WSSR for each triplet of temperatures. For better visibility, only the results with the WSSR 1.5 times the minimum value reached over all temperature triplets are shown. The middle panels show the maps of WSSR for all pairs T_2 and T_3 with fixed T_1 corresponding to the best fit. It should be

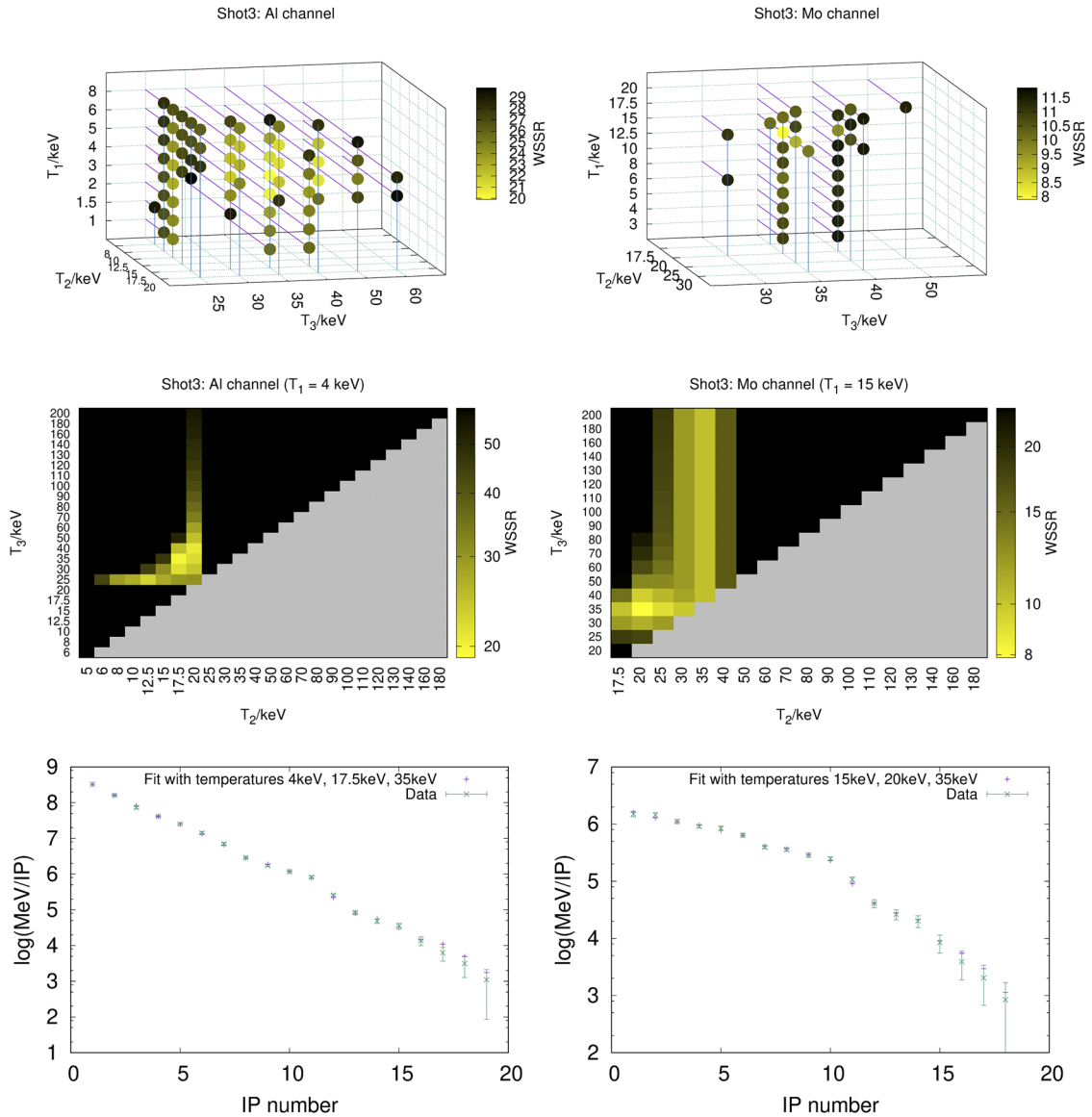

FIG. 9. Shot 3: WSSR for temperature triplets T_1, T_2, and T_3 for the Al filter channel (top left) and the Mo filter channel (top right) and for temperature pairs T_2 and T_3 at fixed T_1 (middle panels). In the bottom panels, the experimental data are shown together with the best fit (minimum WSSR) for the Al (left) and the Mo (right) filter channel.

TABLE II. Best fitting temperature triplets and photon numbers for the Al and the Mo filter channel for the three shots. The temperature ranges corresponding to the WSSR <1.5 times the minimum WSSR are also given (square brackets).

	T_1 (keV)	$N_1\left(\frac{photons}{sr}\right)$	T_2 (keV)	$N_2\left(\frac{photons}{sr}\right)$	T_3 (keV)	$N_3\left(\frac{photons}{sr}\right)$
Shot 1 Al	3 [2–3]	8.6×10^{14}	20 [17.5–20]	7.3×10^{12}	140 [60–200]	1.1×10^{10}
Shot 1 Mo	17.5 [17.5]	8.6×10^{12}	25 [25–40]	1.4×10^{12}	200 [80–200]	6.0×10^{9}
Shot 2 Al	3 [3]	3.2×10^{15}	15 [15]	8.8×10^{12}	90 [60–180]	1.8×10^{10}
Shot 2 Mo	10 [10]	1.9×10^{13}	17.5 [17.5]	4.5×10^{12}	200 [140–200]	5.4×10^{9}
Shot 3 Al	4 [2–8]	1.5×10^{14}	17.5 [10–20]	8.2×10^{12}	35 [30–60]	5.9×10^{11}
Shot 3 Mo	15 [3–17.5]	1.1×10^{13}	20 [17.5–30]	3.3×10^{12}	35 [30–50]	5.1×10^{11}

noted that a constant WSSR along one temperature axis in these maps [e.g., the vertical lines visible in Fig. 9 (right middle panel) for the shot 3 Mo channel at temperatures T_2 = 30 keV, 35 keV, and 40 keV] indicates that the corresponding photon number vanishes, thus resulting in a two-temperature distribution. In the bottom panels, the data measured in the IP layers together with the fit for the temperature triplet resulting in the lowest WSSR are displayed. The left panels in each figure refer to the results from the Al filter channel and the right panels to the results from the Mo filter channel from the same shot. The results are summarized in Table II.

In the first shot, the temperatures that best fit the experimental data are 3 keV, 20 keV, and 140 keV for the Al filter channel and 17.5 keV, 25 keV, and 200 keV for the Mo filter channel. The lowest temperatures are expected to differ for the two channels, as the low energy photons will not reach the IP layers in the case of the Mo filter due to the higher attenuation. Therefore, the intermediate temperature retrieved from the analysis of the Al filter channel should be compared to the low and intermediate temperatures retrieved from the analysis of the Mo filter channel data. In particular, the Al filter channel yields an intermediate temperature of 20 keV, in fairly good agreement with the combination of the retrieved temperatures T_1 = 17.5 keV and T_2 = 25 keV from the analysis of the Mo filter channel. The highest temperatures retrieved from the analysis of the two BSC channels differ significantly due to limitations of the analysis procedure. In fact, the higher temperature is affected by a large error, as can be seen in the top panels in Fig. 7. The WSSR changes only slightly over a large range of highest temperatures T_3. This is mainly due to the low photon flux on highly filtered IP layers that are more sensitive to the T_3 temperature distribution, which is more than two orders of magnitude lower than the photon flux on the intermediate IP layers that are more sensitive to the T_2 temperature distribution (see Table II).

Very similar considerations apply to the second shot. The resulting intermediate temperatures are slightly lower than those in the case of shot 1 (T_2 = 15 keV for the Al filter channel and the combination of T_1 = 10 keV and T_2 = 17.5 keV for the Mo filter channel), consistent with the slightly lower laser power (10.7 TW for shot 1 and 9.7 TW for shot 2). A high-temperature component is also present in shot 2 (90 keV for the Al filter channel and 200 keV for the Mo filter channel).

The results from shot 3 are significantly different from those from the first two shots. The highest temperature of the reconstructed photon distribution is T_3 = 35 keV (for both the Al and the Mo filter channel), significantly lower than the highest temperatures retrieved for the first two shots. In the middle right panel of Fig. 9, the WSSR for T_3 > 40 keV is constant for the temperatures T_2 = 30 keV, 35 keV, and 40 keV. In this case, the minimization procedure for the temperature triplets all yields N_3 = 0, resulting in two-temperature photon distributions with temperatures T_1 and T_2, and therefore, the WSSR is constant. For this shot, the temperatures T_2 and T_3 of the reconstructed photon distributions are in good agreement between the Al/Mo filter channels. Although the photon distribution temperatures cannot be directly related to the fast electron temperatures in our experimental conditions as explained above, the absence of the high-temperature component certainly indicates that lower energy fast electrons are generated in shot 3. This is consistent with the irradiation conditions, as the SSD technique is expected to lower the level of parametric instabilities.

V. CONCLUSIONS

Bremsstrahlung measurements were performed in a shock ignition relevant experiment at LMJ using a BSC detector. The BSC stack was optimized for detecting bremsstrahlung emission from fast electrons, as expected in this intensity regime, with the aim of distinguishing the contributions arising from two fast electron distributions due to SRS and TPD instabilities. The first experimental results clearly show that the designed BSC stack is capable of discriminating variations of x-ray photon distributions typical of this SI regime of interaction. A three-temperature Maxwell–Boltzmann distribution, with temperatures around 2 keV–4 keV, 15 keV–25 keV, and ≥90 keV, respectively, satisfactorily fits the measured bremsstrahlung emission. The results also clearly show that the setup of the BSC

high energy component is sensitive to the change in interaction conditions of the high energy spectral component when SSD is used to reduce instabilities. The determination of the exact temperature value of the high energy component is affected by a large uncertainty due to the low number of photons and will require further optimization that can now be carried out based on this experimental observation. Furthermore, in order to strengthen the correlation between the x-ray spectral features and the original fast electron distributions, the detailed geometrical and physical properties of the target should be taken into account to properly model the bremsstrahlung emission.

ACKNOWLEDGMENTS

The authors acknowledge the support from the Enabling Research Project EUROfusion (Task Agreement No. ENR-IFE19.CEA-01, Grant Agreement No. 633053) funded under the Horizon 2020-Euratom program. The PETAL laser was designed and constructed by CEA under the financial auspices of Conseil Regional d'Aquitaine, the French Ministry of Research, and the European Union. The CRACC diagnostic was designed and commissioned at the LMJ-PETAL facility as a result of the PETAL+ project coordinated by Université de Bordeaux and funded by the French Agence Nationale de la Recherche under Grant No. ANR-10-EQPX-42-01 and the PetaPhys project under Grant No. ANR-10-IDEX-03-02. The LMJ-PETAL experiment presented in this article was supported by Association Lasers et Plasmas and by CEA. The views and opinions expressed herein do not necessarily reflect those of the European Commission.

DATA AVAILABILITY

The data that support the findings of this study are available from the corresponding author upon reasonable request.

REFERENCES

[1]R. Betti, C. D. Zhou, K. S. Anderson, L. J. Perkins, W. Theobald, and A. A. Solodov, "Shock ignition of thermonuclear fuel with high areal density," Phys. Rev. Lett. **98**, 155001 (2007).

[2]W. L. Kruer, *The Physics of Laser-Plasma Interactions*, Frontiers in Physics Vol. 73 (Addison-Wesley Publishing Co., Reading, MA, USA, 1988).

[3]W. Seka, E. A. Williams, R. S. Craxton, L. M. Goldman, R. W. Short, and K. Tanaka, "Convective stimulated Raman scattering instability in UV laser plasmas," Phys. Fluids **27**, 2181 (1984).

[4]K. Tanaka, L. M. Goldman, W. Seka, M. C. Richardson, J. M. Soures, and E. A. Williams, "Stimulated Raman scattering from UV-laser-produced plasmas," Phys. Rev. Lett. **48**, 1179 (1982).

[5]C. Rousseaux, F. Amiranoff, C. Labaune, and G. Matthieussent, "Suprathermal and relativistic electrons produced in laser-plasma interaction at 0.26, 0.53 and 1.05 μm laser wavelength," Phys. Fluids B **4**, 2589 (1992).

[6]G. Cristoforetti, L. Antonelli, S. Atzeni, F. Baffigi, F. Barbato, D. Batani, G. Boutoux, A. Colaitis, J. Dostal, R. Dudzak, L. Juha, P. Koester, A. Marocchino, D. Mancelli, P. Nicolai, O. Renner, J. J. Santos, A. Schiavi, M. M. Skoric, M. Smid, P. Straka, and L. A. Gizzi, "Measurements of parametric instabilities at laser intensities relevant to strong shock generation," Phys. Plasmas **25**, 012702 (2018).

[7]A. B. Langdon, B. F. Lasinski, and W. L. Kruer, "Nonlinear saturation and recurrence of the two-plasmon decay instability," Phys. Rev. Lett. **43**, 1591 (1979).

[8]O. Willi, T. Afshar-rad, S. Coe, and A. Giulietti, "Study of instabilities in long scale-length plasmas with and without laser-beam-smoothing techniques," Phys. Fluids B **2**, 1318 (1990).

[9]T. Afshar-rad, L. A. Gizzi, M. Desselberger, F. Khattak, and O. Willi, "Evidence for whole-beam self-focusing of induced spatially incoherent laser light in large underdense plasma," Phys. Rev. Lett. **68**, 942 (1992).

[10]G. Cristoforetti, L. Antonelli, D. Mancelli, S. Atzeni, F. Baffigi, F. Barbato, D. Batani, G. Boutoux, F. D'Amato, J. Dostal, R. Dudzak, E. Filippov, Y. J. Gu, L. Juha, O. Klimo, M. Krus, S. Malko, A. S. Martynenko, P. Nicolai, V. Ospina, S. Pikuz, O. Renner, J. J. Santos, V. T. Tikhonchuk, J. Trela, S. Viciani, L. Volpe, S. Weber, and L. A. Gizzi, "Time evolution of stimulated Raman scattering and two-plasmon decay at laser intensities relevant for shock ignition in a hot plasma," High Power Laser Sci. Eng. **7**, e51 (2019).

[11]W. Theobald, R. Nora, W. Seka, M. Lafon, K. S. Anderson, M. Hohenberger, F. J. Marshall, D. T. Michel, A. A. Solodov, C. Stoeckl, D. H. Edgell, B. Yaakobi, A. Casner, C. Reverdin, X. Ribeyre, A. Shvydky, A. Vallet, J. Peebles, F. N. Beg, M. S. Wei, and R. Betti, "Spherical strong-shock generation for shock-ignition inertial fusion," Phys. Plasmas **22**, 056310 (2015).

[12]L. Antonelli, J. Trela, F. Barbato, J. Boutoux, P. Nicolaï, D. Batani, V. Tikhonchuk, D. Mancelli, A. Tentori, S. Atzeni, A. Schiavi, F. Baffigi, G. Cristoforetti, S. Viciani, L. A. Gizzi, M. Smid, O. Renner, J. Dostal, R. Dudzak, L. Juha, and M. Krus, "Laser-driven strong shocks with infrared lasers at intensity of 10^{16} W/cm^2," Phys. Plasmas **26**, 112708 (2019).

[13]G. Malka and J. L. Miquel, "Experimental confirmation of ponderomotive-force electrons produced by an ultrarelativistic laser pulse on a solid target," Phys. Rev. Lett. **77**, 75 (1996).

[14]L. Labate, M. Galimberti, A. Giulietti, D. Giulietti, P. Köster, P. Tomassini, and L. A. Gizzi, "Study of forward accelerated fast electrons in ultrashort Ti Kα sources," Appl. Phys. B **86**, 229–233 (2006).

[15]L. Gizzi, D. Batani, V. Biancalana, A. Giulietti, and D. Giulietti, "X-ray emission from thin-foil laser-produced plasmas," Laser Part. Beams **10**, 65–74 (1992).

[16]M. H. Key, M. D. Cable, T. E. Cowan, K. G. Estabrook, B. A. Hammel, S. P. Hatchett, E. A. Henry, D. E. Hinkel, J. D. Kilkenny, J. A. Koch, W. L. Kruer, A. B. Langdon, B. F. Lasinski, R. W. Lee, B. J. MacGowan, J. D. Moody, M. J. Moran, A. A. Offenberger, D. M. Pennington, M. D. Perry, T. J. Phillips, T. C. Sangster, M. S. Singh, M. A. Stoyer, M. Tabak, G. L. Tietbohl, M. Tsukamoto, K. Wharton, and S. C. Wilks, "Hot electron production and heating by hot electrons in fast ignitor research," Phys. Plasmas **5**, 1966 (1998).

[17]G. Cristoforetti, M. P. Anania, A. Y. Faenov, A. Giulietti, D. Giulietti, S. B. Hansen, P. Koester, L. Labate, T. Levato, T. A. Pikuz, and L. A. Gizzi, "Spatially resolved analysis of Kα x-ray emission from plasmas induced by a femtosecond weakly relativistic laser pulse at various polarizations," Phys. Rev. E **87**, 023103 (2013).

[18]P. Köster, K. Akli, D. Batani, S. Baton, R. G. Evans, A. Giulietti, D. Giulietti, L. A. Gizzi, J. S. Green, M. Koenig, L. Labate, A. Morace, P. Norreys, F. Perez, J. Waugh, N. Woolsey, and K. L. Lancaster, "Experimental investigation of fast electron transport through Kα imaging and spectroscopy in relativistic laser–solid interactions," Plasma Phys. Controlled Fusion **51**, 014007 (2009).

[19]K. B. Wharton, S. P. Hatchett, S. C. Wilks, M. H. Key, J. D. Moody, V. Yanovsky, A. A. Offenberger, B. A. Hammel, M. D. Perry, and C. Joshi, "Experimental measurements of hot electrons generated by ultraintense (>10^{19} W/cm^2) laser–plasma interactions on solid-density targets," Phys. Rev. Lett. **81**, 822 (1998).

[20]S. Baton, A. Colaitis, C. Rousseaux, G. Boutoux, S. Brygoo, L. Jacquet, M. Koenig, D. Batani, A. Casner, E. Le Bel, D. Raffestin, V. Tikhonchuk, J. Trela, C. Reverdin, L. Le-Deroff, W. Theobald, G. Cristoforetti, L. A. Gizzi, P. Koester, L. Labate, and K. Shigemori, "Preliminary results from the LMJ-PETAL experiment on hot electrons characterization in the context of shock ignition," High Energy Density Phys. **36**, 100796 (2020).

[21]J. Trela, W. Theobald, K. S. Anderson, D. Batani, R. Betti, A. Casner, J. A. Delettrez, J. A. Frenje, Y. Glebov, X. Ribeyre, A. A. Solodov, M. Stoeckl, and C. Stoeckl, "The control of hot-electron preheat in shock-ignition implosions," Phys. Plasmas **25**, 052707 (2018).

[22]C. D. Chen, J. A. King, M. H. Key, K. U. Akli, F. N. Beg, H. Chen, R. R. Freeman, A. Link, A. J. Mackinnon, A. G. MacPhee, P. K. Patel, M. Porkolab, R. B. Stephens, and L. D. Van Woerkom, "A bremsstrahlung spectrometer using K-edge

and differential filters with image plate dosimeters," Rev. Sci. Instrum. **79**, 10E305 (2008).
[23]C. Courtois, R. Edwards, A. Compant La Fontaine, C. Aedy, S. Bazzoli, J. L. Bourgade, J. Gazave, J. M. Lagrange, O. Landoas, L. Le Dain, D. Mastrosimone, N. Pichoff, G. Pien, and C. Stoeckl, "Characterisation of a MeV bremsstrahlung x-ray source produced from a high intensity laser for high areal density object radiography," Phys. Plasmas **20**, 083114 (2013).
[24]R. H. H. Scott, E. L. Clark, F. Pérez, M. J. V. Streeter, J. R. Davies, H.-P. Schlenvoigt, J. J. Santos, S. Hulin, K. L. Lancaster, S. D. Baton, S. J. Rose, and P. A. Norreys, "Measuring fast electron spectra and laser absorption in relativistic laser–solid interactions using differential bremsstrahlung photon detectors," Rev. Sci. Instrum. **84**, 083505 (2013).
[25]Y. J. Rhee, S. M. Nam, J. Peebles, H. Sawada, H. Wei, X. Vaisseau, T. Sasaki, L. Giuffrida, S. Hulin, B. Vauzour, J. J. Santos, D. Batani, H. S. McLean, P. K. Patel, Y. T. Li, D. W. Yuan, K. Zhang, J. Y. Zhong, C. B. Fu, N. Nua, K. Li, Y. Zhang, J. Q. Zhu, I. J. Kim, J. H. Jeon, T. M. Jeong, I. W. Choi, H. W. Lee, J. H. Sung, S. K. Lee, and C. H. Nam, "Spectral tomographic analysis of bremsstrahlung x-rays generated in a laser produced plasma," Laser Part. Beams **34**, 645–654 (2016).
[26]O. Klimo, J. Psikal, V. T. Tikhonchuk, and S. Weber, "Two-dimensional simulations of laser–plasma interaction and hot electron generation in the context of shock-ignition research," Plasma Phys. Controlled Fusion **56**, 055010 (2014).
[27]S. Agostinelli, J. Allison, K. Amako, J. Apostolakis, H. Araujo, P. Arce, M. Asai, D. Axen, S. Banerjee, G. Barrand, F. Behner, L. Bellagamba, J. Boudreau, L. Broglia, A. Brunengo, H. Burkhardt, S. Chauvie, J. Chuma, R. Chytracek, G. Cooperman, G. Cosmo, P. Degtyarenko, A. Dell'Acqua, G. Depaola, D. Dietrich, R. Enami, A. Feliciello, C. Ferguson, H. Fesefeldt, G. Folger, F. Foppiano, A. Forti, S. Garelli, S. Giani, R. Giannitrapani, D. Gibin, J. J. Gómez Cadenas, I. González, G. Gracia Abril, G. Greeniaus, W. Greiner, V. Grichine, A. Grossheim, S. Guatelli, P. Gumplinger, R. Hamatsu, K. Hashimoto, H. Hasui, A. Heikkinen, A. Howard, V. Ivanchenko, A. Johnson, F. W. Jones, J. Kallenbach, N. Kanaya, M. Kawabata, Y. Kawabata, M. Kawaguti, S. Kelner, P. Kent, A. Kimura, T. Kodama, R. Kokoulin, M. Kossov, H. Kurashige, E. Lamanna, T. Lampén, V. Lara, V. Lefebure, F. Lei, M. Liendl, W. Lockman, F. Longo, S. Magni, M. Maire, E. Medernach, K. Minamimoto, P. Mora de Freitas, Y. Morita, K. Murakami, M. Nagamatu, R. Nartallo, P. P. Nieminen, T. Nishimura, K. Ohtsubo, M. M. Okamura, S. O'Neale, Y. Oohata, K. Paech, J. Perl, A. Pfeiffer, M. G. Pia, F. Ranjard, A. Rybin, S. Sadilov, E. Di Salvo, G. Santin, T. Sasaki, N. Savvas, Y. Sawada, S. Scherer, S. Sei, V. Sirotenko, D. Smith, N. Starkov, H. Stoecker, J. Sulkimo, M. Takahata, S. Tanaka, E. Tcherniaev, E. Safai Tehrani, M. Tropeano, P. Truscott, H. Uno, L. Urban, P. Urban, M. Verderi, A. Walkden, W. Wander, H. Weber, J. P. Wellisch, T. Wenaus, D. C. Williams, D. Wright, T. Yamada, H. Yoshida, and D. Zschiesche, "GEANT4—A simulation toolkit," Nucl. Instrum. Methods Phys. Res., A **506**, 250–303 (2003).
[28]F. Salvat, J. M. Fernandez-Varea, and J. Sempau, *PENELOPE-2011: A Code System for Monte Carlo Simulation of Electron and Photon Transport*, OECD NEA Data Bank/NSC DOC(2011)/5 (Organisation for Economic Co-Operation and Development-Nuclear Energy Agency, Issy-les-Moulineaux, France, 2011).
[29]L. Pandola, C. Andenna, and B. Caccia, "Validation of the GEANT4 simulation of bremsstrahlung from thick targets below 3 MeV," Nucl. Instrum. Methods Phys. Res., B **350**, 41–48 (2015).
[30]G. J. Williams, B. R. Maddox, H. Chen, S. Kojima, and M. Millecchia, "Calibration and equivalency analysis of image plate scanners," Rev. Sci. Instrum. **85**, 11E604 (2014).
[31]B. Hidding, G. Pretzler, M. Clever, F. Brandl, F. Zamponi, A. Lübcke, T. Kämpfer, I. Uschmann, E. Förster, U. Schramm, R. Sauerbrey, E. Kroupp, L. Veisz, K. Schmid, S. Benavides, and S. Karsch, "Novel method for characterizing relativistic electron beams in a harsh laser–plasma environment," Rev. Sci. Instrum. **78**, 083301 (2007).
[32]G. Boutoux, N. Rabhi, D. Batani, A. Binet, J.-E. Ducret, K. Jakubowska, J.-P. Nègre, C. Reverdin, and I. Thfoin, "Study of imaging plate detector sensitivity to 5–18 MeV electrons," Rev. Sci. Instrum. **86**, 113304 (2015).
[33]G. Boutoux, D. Batani, F. Burgy, J.-E. Ducret, P. Forestier-Colleoni, S. Hulin, N. Rabhi, A. Duval, L. Lecherbourg, C. Reverdin, K. Jakubowska, C. I. Szabo, S. Bastiani-Ceccotti, F. Consoli, A. Curcio, R. De Angelis, F. Ingenito, J. Baggio, and D. Raffestin, "Validation of modelled imaging plates sensitivity to 1–100 keV x-rays and spatial resolution characterisation for diagnostics for the "PETawatt Aquitaine Laser," Rev. Sci. Instrum. **87**, 043108 (2016).